Hindawi
International Journal of Photoenergy
Volume 2018, Article ID 2473152, 9 pages
https://doi.org/10.1155/2018/2473152

Research Article

A Solution-Processed Tetra-Alkoxylated Zinc Phthalocyanine as Hole Transporting Material for Emerging Photovoltaic Technologies

Gloria Zanotti,[1] **Giuseppe Mattioli**,[1] **Anna Maria Paoletti**,[1] **Giovanna Pennesi**,[1] **Daniela Caschera**,[2] **Nitzan Maman**,[3,4] **Iris Visoly-Fisher**,[3,4] **Ravi K. Misra**,[5] **Lioz Etgar**,[5] **and Eugene A. Katz**[3,4]

[1]*Istituto di Struttura della Materia (ISM), CNR, Via Salaria km 29.300, 00015 Monterotondo, Rm, Italy*
[2]*Istituto per lo Studio dei Materiali Nanostrutturati (ISMN), CNR, Via Salaria km 29.300, 00015 Monterotondo, Rm, Italy*
[3]*Department of Solar Energy and Environmental Physics, Swiss Institute for Dryland Environmental and Energy Research, Jacob Blaustein Institutes for Desert Research, Ben-Gurion University of the Negev, Midreshet Ben-Gurion 8499000, Israel*
[4]*Ilse Katz Institute for Nanoscale Science and Technology, Ben-Gurion University of the Negev, 84105 Be'er Sheva, Israel*
[5]*Center for Applied Chemistry, the Institute of Chemistry, The Hebrew University of Jerusalem, Jerusalem, Israel*

Correspondence should be addressed to Gloria Zanotti; gloria.zanotti@ism.cnr.it

Received 5 June 2018; Revised 30 August 2018; Accepted 6 September 2018; Published 13 November 2018

Academic Editor: Yanfa Yan

A tetra-*n*-butoxy zinc phthalocyanine ($(n\text{-BuO})_4$ZnPc has been synthesized in a single step, starting from commercial precursors, and easily purified. The molecule can be solution processed to form an effective and inexpensive hole transport layer for organic and perovskite solar cells. These appealing features are suggested by the results of a series of chemical, optical, and voltammetric characterizations of the molecule, supported by the results of ab initio simulations. Preliminary measurements of $(n\text{-BuO})_4$ZnPc-methylammonium lead triiodide perovskite-based devices confirm such suggestion and indicate that the interface between the photoactive layer and the hole transporting layer is characterized by hole-extracting and electron-blocking properties, potentially competitive with those of other standards de facto in the field of organic hole transport materials, like the expensive Spiro-OMeTAD.

Hole transporting layers (HTLs) have demonstrated to be fundamental to achieve high efficiency and long-term durability in new-generation hybrid organic photovoltaic devices. They must provide a good chemical stability, a high hole mobility, and an ideal matching between their HOMO levels and the valence band maximum of the active layer, promoting an efficient collection of photogenerated holes at the electrode. In particular, they have been extensively employed in perovskite solar cells (PSCs) [1–3], contributing to boost their impressive evolution in the last ten years from an initial 3.8% [4] to a 22.1% [5] certified efficiency. More specifically, the presence of a HTL increases the extraction rate of photogenerated holes from the perovskite film and improves their transport to the back contact metal electrode. This, in turn, minimizes recombination losses and charge-induced decomposition of the active layer, thus increasing the overall PSC performance. Several small molecules, polymers, and inorganic materials have been studied and tested for this purpose [6]. 2,2′,7,7′-Tetrakis(N,N-di-*p*-methoxyphenilamine)-9,9′-spirobifluorene (Spiro-OMeTAD) and poly(triarylamine) (PTAA) are among the most effective organic hole transporting materials (HTMs), yielding highly efficient PSCs [7, 8]. However, their synthesis requires complex multistep procedures resulting in a significant increase of the device price. Phthalocyanines (Pcs) and similar macrocyclic compounds are well-known p-type organic semiconductors and have found applications as hole transporters in organic photovoltaics (OPV) [9, 10] and in organic field effect transistors (OFETs) [11] due to their high chemical stability, large conjugated π-system, and tunable optical/electrochemical properties through chemical functionalization. Such well-known features promoted their use as HTLs in PSCs, and several examples have been reported for vacuum-evaporated and spin-coated layers, depending on their molecular structure [12–15]. Recently, an impressive 17.5% efficiency scored by tetra-5-hexyl-2,2′-bisthiophene zinc phthalocyanine in a mixed-ion perovskite solar cell has been reported by Cho et al. [16], due to the effect of a favorable packing of the molecule on its transport properties.

Aimed at pushing further down the fabrication cost, a key feature of OPV and PSC technologies, we developed a solution-processable HTL with the target molecule prepared in a one-step synthesis from easily available, cheap precursors. The molecule is a symmetric tetra-*n*-butoxy-substituted zinc phthalocyanine, hereinafter named $(n\text{-BuO})_4\text{ZnPc}$.

Its electron-donating alkoxy peripheral substituents have been chosen to accomplish two main tasks: (i) tuning the $(n\text{-BuO})_4\text{ZnPc}$ electronic properties, thus optimizing the alignment of HOMO-LUMO levels to the perovskite band edges, and (ii) assuring the $(n\text{-BuO})_4\text{ZnPc}$ processability within a device by formation of spin-coated homogeneous films with favorable molecular packing.

$(n\text{-BuO})_4\text{ZnPc}$ has been synthesized with a 53% yield in a one-step reaction, using commercially available 4-*n*-butoxyphthalonitrile and ZnCl_2 as templating salt, as shown in Scheme 1.

The crude has been purified by filtration on silica gel using dichloromethane and THF as eluents, and the resulting purple crystalline solid has been characterized by different techniques. UV-Vis spectra have been measured in transmission mode both in solution (solid black line) and as spin-coated film (solid red line), as shown in Figure 1(a).

The solution spectrum in acetonitrile is dominated by the typical phthalocyanine Q-band absorption, with its maximum peak at 675 nm and a shoulder peak at 610 nm, which was also observed in gas-phase measurements of unsubstituted ZnPc [17]. The latter should therefore be considered as part of the vibrational envelope of the $S_0 \rightarrow S_1{}^*$ transition rather than a fingerprint of H-type (cofacial) aggregation of the molecules. As expected, the same Q-band is much broader in the case of the $(n\text{-BuO})_4\text{ZnPc}$ film and composed by two redshifted bands centered at 692 and 737 nm. This behavior is compatible with an "edge-to-edge" macrocycle arrangement typical of J-type (coplanar) aggregation [18, 19]. The steady-state emission spectrum of a $(n\text{-BuO})_4\text{ZnPc}$ solution in acetonitrile, recorded at $\lambda_{\text{ex}} = 600$ nm, shows a maximum centered at 686 nm, with a small Stokes shift of 11 nm. The related time-correlated single-photon counting measurements, shown in Figure 1(b), were performed at 686 nm, and the resulting decay curve was monoexponentially fitted, providing a $\tau_1 = 2.4$ ns. An optical band gap of 1.82 eV was estimated from the interception of the normalized absorption and emission spectra. This result, combined with cyclovoltammetric measurements, allowed to estimate the reduction potentials of the $(n\text{-BuO})_4\text{ZnPc}/(n\text{-BuO})_4\text{ZnPc}^+$ and $(n\text{-BuO})_4\text{ZnPc}^-/(n\text{-BuO})_4\text{ZnPc}$ couples indicated as E_{HOMO} and E_{LUMO}, respectively. The optical and electrochemical characterizations of the compound are summarized in Table 1.

To evaluate the processability of $(n\text{-BuO})_4\text{ZnPc}$ in terms of quality, homogeneity, and roughness of its films, atomic force microscopy topographic measurements have been performed. Molecular films have been prepared by spin coating, using 20 mg/ml of toluene solutions on nonconductive glass plates. Large-area scans of $5\,\mu\text{m} \times 5\,\mu\text{m}$ surfaces, an example is reported in Figure 2, indicated a flat and uniform film in the explored regions, suggesting that the molecule can be successfully layered in a planar device. The root mean square roughness of the reported film was found to be 4.94 nm, with an average height of 4.76 nm and a surface skewness of 0.24 nm. The presence of rare overlying crystallites up to 288 nm (143 nm in Figure 2) has sometimes been detected.

Optical and electrochemical measurements are in agreement with ab initio results based on density functional theory (DFT) [20] and are compared to simulations of Spiro-OMeTAD and tetra-tert-butyl zinc phthalocyanine (hereinafter referred to as $(t\text{-Bu})_4\text{ZnPc}$) properties, chosen as internal standards. The theoretical results are summarized in Table 2 and support the idea that the *n*-butoxy substituents have a combined structural and electronic effect on the properties of $(n\text{-BuO})_4\text{ZnPc}$ molecular films.

The peripheral *n*-butoxy substituents induce an extension of the spatial distribution of the $(n\text{-BuO})_4\text{ZnPc}$ HOMO orbital responsible for the transport of holes to the back electrode, as opposed to the *t*-Bu substituents of the similar $(t\text{-Bu})_4\text{ZnPc}$ molecule (see Figure 3). Such a resonant effect is accompanied with the strong electron-donating behavior of O-R groups that stabilizes positive-charge carriers and induces a 0.25 eV rising of the HOMO with respect to the weaker alkyl substituents. This indication is confirmed by an analysis of the charge displacement induced by a hole injected in $(n\text{-BuO})_4\text{ZnPc}$ (Figure 3), which underlines the role of the peripheral *n*-butoxy substituents. Theoretical estimates of reduction potentials in acetonitrile [21] are displayed in Figure 4, left side, and offer further comparison between the properties of $(n\text{-BuO})_4\text{ZnPc}$ and Spiro-OMeTAD. A calculated E_{HOMO} value of −5.23 eV (vs vacuum) in the case of $(n\text{-BuO})_4\text{ZnPc}$ approaches the −4.96 eV value estimated in the case of Spiro-OMeTAD, whereas a corresponding reduction potential of −3.31 eV for the E_{LUMO} value is suitable for blocking free electrons that diffuse in the active perovskite layer. These results confirm that $(n\text{-BuO})_4\text{ZnPc}$ is a suitable hole transport material for organic and perovskite solar cells. In particular, as shown in Figure 4, right side, in a methylammonium lead triiodide-based solar cell, the −5.18 eV oxidation potential of the phthalocyanine allows the hole transport from the photoactive layer from the perovskite/HTL interface to the gold electrode, while the reduction potential, higher than that of the perovskite, prevents the electrons to diffuse back and recombine on it.

As a proof of concept, several $\text{CH}_3\text{NH}_3\text{PbI}_3$ PSCs with an active area of 0.04 cm^2 have been prepared using a two-step deposition protocol: a widely employed device architecture

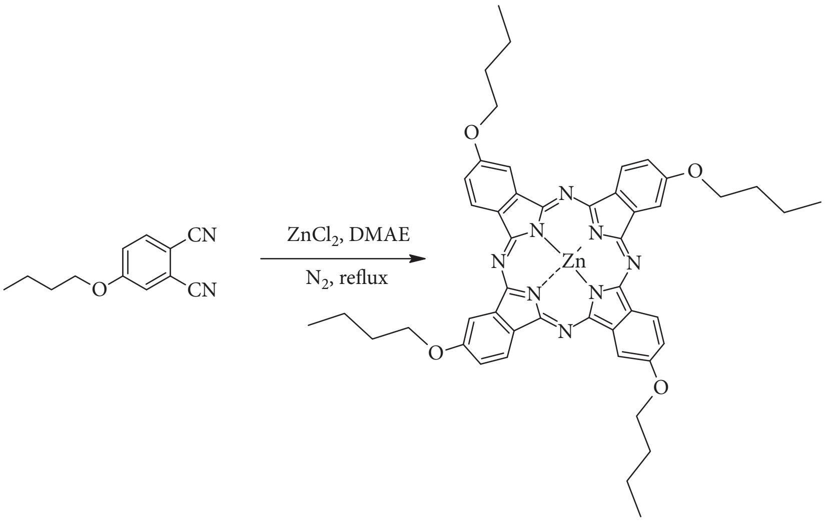

Scheme 1: Synthesis of $(n\text{-BuO})_4$ZnPc in dimethylaminoethanol (DMAE).

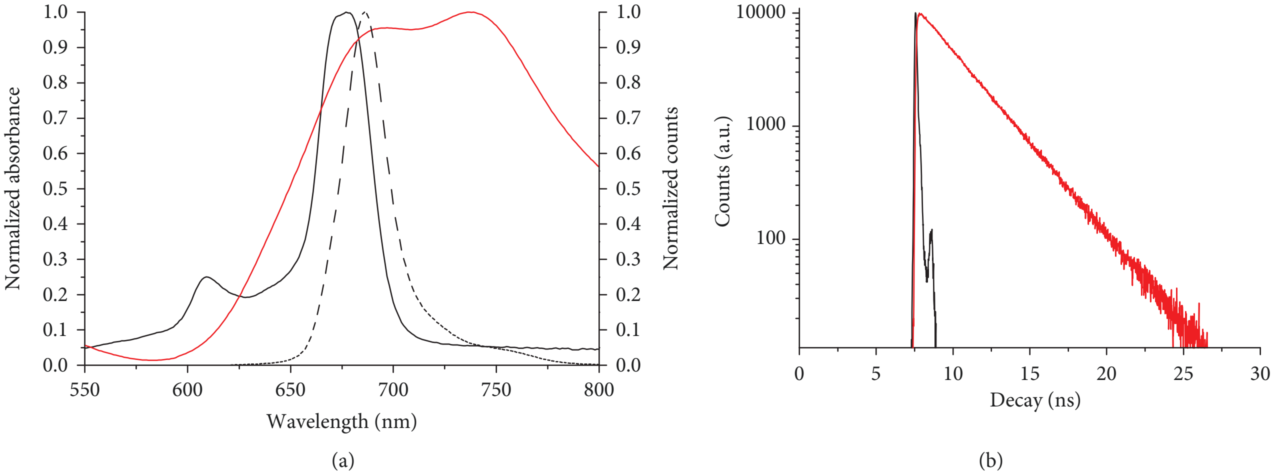

(a)

(b)

Figure 1: (a) Black solid line: normalized $(n\text{-BuO})_4$ZnPc UV-Vis absorption in acetonitrile. Black dashed line: emission spectrum in acetonitrile. Red solid line: Q-band absorption spectrum of a spin-coated film on nonconductive glass. (b) Red solid line: $(n\text{-BuO})_4$ZnPc fluorescence decay in acetonitrile. Black solid line: prompt.

Table 1: Optical and electrochemical properties of $(n\text{-BuO})_4$ZnPc.

	$\lambda_{\max}$ (nm)[a]	E_{0-0} (eV)[b]	$E(1)_{1/2\text{ox}}$ (V)[c]	E_{HOMO} (eV)[d]	E_{LUMO} (eV)[e]
$(n\text{-BuO})_4$ZnPc	675	1.82	0.741	−5.18	−3.36

[a] Absorption maximum in acetonitrile. [b] 0-0 transition energy. [c] Solvent: acetonitrile vs NHE. [d] $E_{\text{HOMO}} = E(1)_{1/2\text{ox}} + 4.44$ (eV) [16]. [e] $E_{\text{LUMO}} = E_{\text{HOMO}} + E_{0-0}$.

with a mesoporous TiO$_2$ electron transporting layer (ETL) and a tert-butylpyridine- (TBP-), lithium bis(trifluoromethanesulfonyl)imide- (LiTFSI-), and tris(2-(1H-pyrazol-1-yl)-4-tert-butylpyridine)-cobalt(III) tris(bis(trifluoromethylsulfonyl)imide))-doped HTL has been used. Spiro-OMeTAD control cells have also been prepared and measured as benchmarks. The obtained data have been subjected to the Peirce's criterion [22] to discard anomalous results. The phthalocyanine scored average efficiencies of 6.06% ± 0.74 (forward bias) and 9.00% ± 0.21 (reverse bias), while 6.75% ± 0.19 (forward bias) and 8.61% ± 0.60 (reverse bias) are the average values obtained using Spiro-OMeTAD. These values, along with the averaged V$_{oc}$, J$_{sc}$, and FF, are reported in Table 3.

Open-circuit voltages average around 0.91 V for both the HTMs, with acceptable standard deviations. Values around 1.0 V are reported in several articles for $CH_3NH_3PbI_3$-based solar devices [23, 24]; our 10% discrepancy may be due to several factors such as a large reverse saturation current occurring because of a high recombination rate at the TiO$_2$/perovskite and HTL/perovskite interfaces and to the presence of pinholes in the charge transport layers that create small short circuits with the metal contacts. J$_{sc}$ and the fill factor

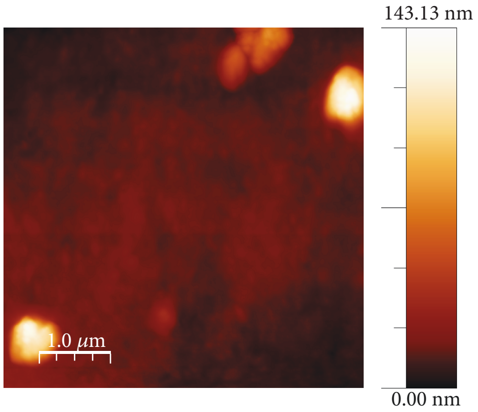

Figure 2: 5 μm × 5 μm AFM image of a (n-BuO)$_4$ZnPc film on nonconductive glass. The color scale ranges from 0 nm (black) to 143 nm (white).

Table 2: HOMO (LUMO) values of isolated molecules calculated at the B3LYP level of theory and E_{HOMO} (E_{LUMO}) voltammetric potentials of the same molecules in CH_3CN calculated at the M06-2X level of theory in the case of (n-BuO)$_4$ZnPc, (t-Bu)$_4$ZnPc, and Spiro-OMeTAD. Oxidation and reduction potentials have been calculated as ΔG values between neutral and charged species, as detailed in [21].

	HOMO (eV)	LUMO (eV)	E_{HOMO} (eV)	E_{LUMO} (eV)
(n-BuO)$_4$ZnPc	−4.95	−2.89	−5.23	−3.31
(t-Bu)$_4$ZnPc	−5.10	−2.96	−5.31	−3.72
Spiro-OMeTAD	−4.61	−1.14	−4.96	−1.63

have lower values than the state-of-the-art and high standard deviations, indicating that the examined batches are subjected to some degree of structural inhomogeneity likely ascribable to the quality of the perovskite layer in terms of crystallinity and evenness.

The current density-voltage ($J - V$) curves and the principal photovoltaic parameters of the best n-(BuO)$_4$ZnPc- and Spiro-OMeTAD-based cells are reported in Figures 5(a) and 5(b), respectively.

Both devices show a remarkable hysteresis with consistent performance discrepancies depending on the scan direction, mostly ascribable to differences in J_{sc} and fill factors. No investigations have yet been performed to rationalize this phenomenon in this specific case; but according to the literature, it can be caused by a number of factors such as scan direction and rate, cell preconditioning, and device architecture [25, 26]. As frequently reported, these cells yielded a higher PCE in reverse bias scans rather than in forward bias scans, likely due to the uprising of dynamic trapping and detrapping processes of charge carriers at the perovskite/HTL and perovskite/ETL interfaces and to ion migration that alters the interfacial energy barriers and consequently modifies their height for the carrier collection [27]. The external quantum efficiency (EQE) spectra, shown in Figure 6, have been recorded between 300 and 850 nm.

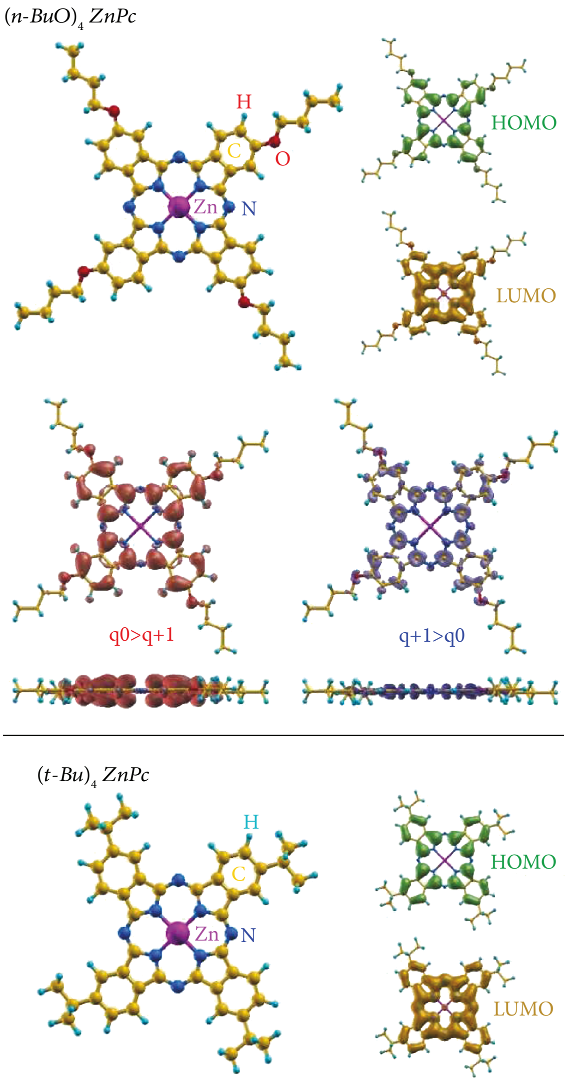

Figure 3: (a) Optimized geometry and $|\Psi|^2$ plots of frontier orbitals of (n-BuO)$_4$ZnPc. Difference density maps (positive and negative values, top and side views) of the charge density of (n-BuO)$_4$ZnPc and [(n-BuO)$_4$ZnPc]$^+$ sampled at 0.0005 electrons/Å^3. Charge is depleted from red regions, basically corresponding to the (n-BuO)$_4$ZnPc HOMO, when the molecule is oxidized. Part of such depleted charge is accumulated in blue regions, mainly localized in the molecular σ plane. Such accumulation of charge around the nuclei is connected with the lower availability of electrons in positive molecular ions for further ionization processes. (b) Optimized geometry and $|\Psi|^2$ plots of frontier orbitals of (t-Bu)$_4$ZnPc.

The photocurrent onset is around 760 nm in both cases, which is in agreement with the 1.55 eV band gap of $CH_3NH_3PbI_3$. In the Spiro-based device, we observe a maximum efficient charge extraction at 570 nm (EQE = 63%), while the phthalocyanine-based cell peaks at 540 nm (EQE = 58%).

For both Spiro-OMeTAD and (n-BuO)$_4$ZnPc, the integrated photocurrent is lower than the averaged one measured in the JV curves. This effect can occur in many different photovoltaic devices and may be due to several factors [28]. In

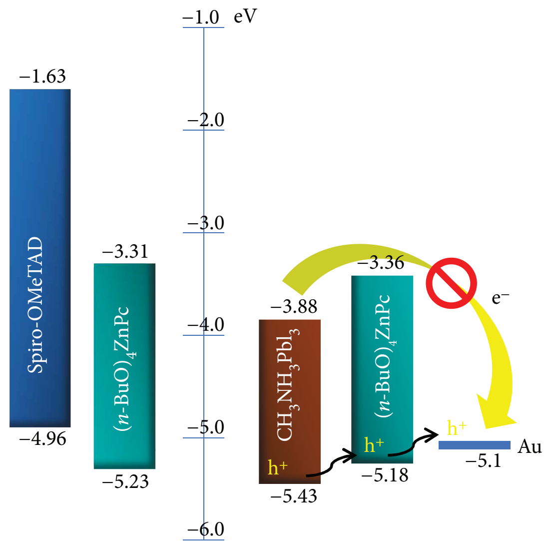

Figure 4: Left side: theoretically estimated reduction potentials of $(n\text{-BuO})_4$ZnPc and Spiro-OMeTAD. Right side: energetic positioning of $(n\text{-BuO})_4$ZnPc within a PSC.

particular, a significant role may be played by a difference in intensity of the incident light in EQE and JV measurement setups (in orders of magnitude). This points to the sublinear dependence of photocurrent in both cells [29] and need for further optimization of current collection and in particular the cell contact system (including contact/conducting layer interfaces). These preliminary evidences suggest that there is wide room for performance improvements focusing the attention on the optimization of the cell construction, which was beyond our initial goal. Nevertheless, in a nonoptimized device, our phthalocyanine-based HTL is capable of forming an interface with the photoactive layer characterized by hole-extracting and electron-blocking properties. These promising results can be further improved with a careful study of the layer deposition parameters and of the dopant ratio to enhance its hole transport properties.

Since we have stressed the importance of lowering the fabrication costs of novel hole transport materials to foresee their future commercialization, we propose a cost-per-gram analysis as a function of the synthetic complexity of $(n\text{-BuO})_4$ZnPc and compare the obtained results with the current price of Spiro-OMeTAD. We point out that moving from lab to fab requires a complete cost analysis that must include parameters like energy, facility maintenance and personnel costs, taxes, and other charges that we have not taken into account. The total material cost (in euros) for our hole transport material has been estimated according to a paper published in 2013 by Osedach et al. [30]. For the sake of simplicity, Sigma-Aldrich has been chosen as the only supplier for reagents, solvents, and purification materials with the exception of 4-*n*-butoxyphthalonitrile that has been quoted from TCI chemicals. In all cases, the bulkiest batches available on the online catalogs have been considered—the list of which is reported in table I in the supplementary materials. The costs of our synthesis have been estimated assuming linearity when scaling the procedure from grams to kilograms, calculating the required amounts of chemicals to produce 1 kg of $(n\text{-BuO})_4$ZnPc in a 53% yield (see the synthesis flowchart in Figure S3 in the supplementary materials) and multiplying them by the respective prices. The resulting costs for reagents, solvents, and purification materials are reported in Table 4, given as euro per gram of the synthesized product.

Given that the experimental protocol can be further optimized and that solvents and reagents can be partially recovered and recycled, two total costs are provided. The "worst-case scenario" (wcs) accounts that any unreacted reagent and all the purification materials are lost as wastes. In the "best-case scenario" (bcs), the purification costs are not included because the chromatographic filtration is replaced by a vacuum treatment (10–3 mmHg at 250°C) that completely avoids the use of silica gel and solvents. Even if we did not include them in our analysis, it is worth to mention that diminishing the amount of wastes is beneficial for reducing their disposal costs.

Spiro-OMeTAD is commercially available and has been quoted from three suppliers as reported in table II in the supplementary materials. With respect to the less-expensive batch, supplied by Sigma-Aldrich at 242.40 €/g, our molecule is 2.8 times cheaper in the worst-case scenario and 3.3 times cheaper in the best-case scenario. Since a large-scale production requires kilograms of input reagents and 4-*n*-butoxyphthalonitrile is sold in 5 g batches at the most, we requested a bulk quotation for a batch of 1 kg, reducing its price from 42.40 €/g to 17.50 €/g. The recalculated synthesis costs, given as euro per gram of synthesized product, are summarized in Table 5.

In this way, $(n\text{-BuO})_4$ZnPc results to be 7.9 times cheaper than Spiro in the best-case scenario, and given the limited number of suppliers that we have taken into consideration and the possibility to request bulk quotations of all the other materials, we are confident that its fabrication costs can be further lowered.

In conclusion, we have synthesized and characterized an easily processable, symmetrically tetrasubstituted zinc phthalocyanine, which is a cheap and promising hole transporting material for new-generation photovoltaics. We have also provided a first proof of concept assessment of its implementation in perovskite solar cells as proof of concept, obtaining promising results even in nonoptimized devices. We suggest therefore that improvements in the cell construction as well as the optimization of the molecular layer can promote $(n\text{-BuO})_4$ZnPc as a possible alternative to commercially available organic p-type semiconductors thanks to its straightforward, potentially scalable, and less-expensive synthetic procedure.

1. Experimental and Computational Details

1.1. $(n\text{-BuO})_4$ZnPc Synthesis and Characterization. $ZnCl_2$ and all the solvents (RPE grade) were purchased from Carlo Erba except for N,N-dimethylethanolamine (99.5%) which was purchased from Aldrich. Acetonitrile was distilled over calcium hydride. 4-*n*-Butoxyphthalonitrile (95%) was purchased from Tokyo Chemical Industry Co. (TCI). 1,5-Diazabicyclo[5.4.0]undec-5-ene (DBU) (≥99%) was purchased from Fluka. Reactions were monitored by thin-layer

Table 3: Average values of the main photovoltaic characteristics of $(n\text{-BuO})_4$ZnPc and Spiro-OMeTAD.

HTM		V_{oc} (V)	J_{sc} (mA/cm^2)	FF (%)	PCE (%)
$(n\text{-BuO})_4$ZnPc	Forward bias	0.896 ± 0.009	12.1 ± 1.2	57.0 ± 3.1	$6.06\% \pm 0.74$
	Reverse bias	0.928 ± 0.04	14.5 ± 1.9	61.8 ± 2.6	$9.00\% \pm 0.21$
Spiro-OMeTAD	Forward bias	0.903 ± 0.02	13.6 ± 0.9	55.2 ± 4.0	$6.75\% \pm 0.19$
	Reverse bias	0.928 ± 0.04	14.5 ± 1.9	61.8 ± 2.6	$8.61\% \pm 0.60$

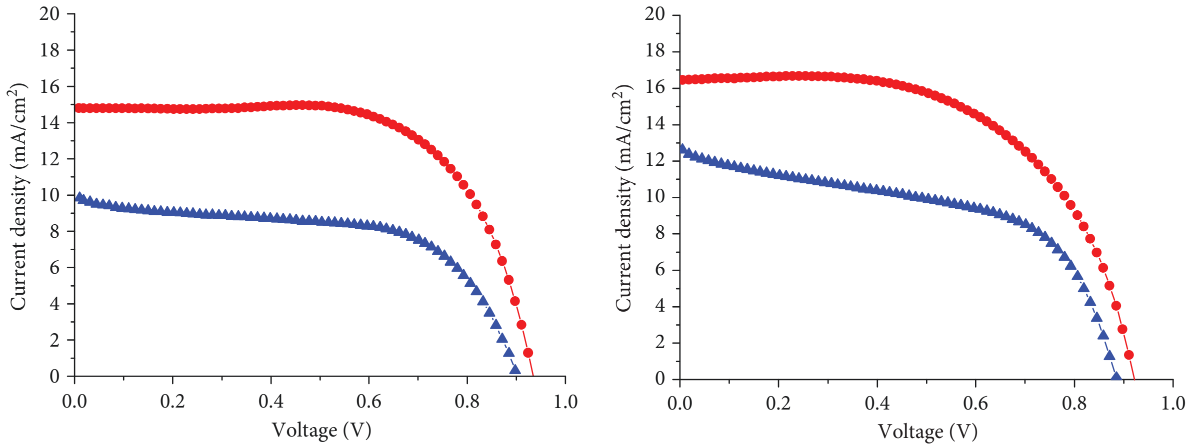

	Voc (V)	Jsc (mA/cm2)	FF (%)	PCE (%)
Forward	0.901	10.4	58.8	5.54
Reverse	0.934	14.8	66.4	9.15

(a)

	Voc (V)	Jsc (mA/cm2)	FF (%)	PCE (%)
Forward	0.888	14.2	52.8	6.62
Reverse	0.92	16.5	58.6	8.88

(b)

Figure 5: J-V characteristics of (a) $(n\text{-BuO})_4$ZnPc and (b) Spiro-OMeTAD-based PSCs.

chromatography (TLC) employing a polyester layer coated with 250 mm F254 silica gel. The crude purification was performed by filtration using silica gel Carlo Erba Reactifs SDS 60A C.C. 35–70 mm and dichloromethane and THF as eluents. To perform the fluorescence measurements, a further purification has been performed by size exclusion chromatography using Bio-Beads S-X Resin (Bio-Rad) as the stationary phase and THF as the mobile phase. ^{1}H NMR spectra were recorded in THF d8 on a Bruker AVANCE 600 NMR spectrometer operating at a proton frequency of 600.13 MHz; chemical shifts (δ) are given in ppm relative to the residual solvent peaks of the deuterated solvent (3.58, 1.73 ppm). Infrared spectra were recorded on a Shimadzu FT-IR prestige-21 spectrometer using an attenuated total reflectance (ATR) unit. All the UV-Vis measurements were performed in direct transmission mode. Absorption spectra of 10^{-5} M solution in acetonitrile were recorded on a PerkinElmer LAMBDA 950 UV-Vis/NIR spectrophotometer, while transparent sensitized films have been analyzed using a Cary 5000 UV-Vis-NIR spectrophotometer (Agilent Technologies). MALDI-TOF spectra have been recorded at Toscana Life Sciences facility in a MALDI-TOF/TOF Ultraflex III (Bruker) using α-cyano-4-hydroxycinnamic acid (HCCA) as matrix. Isotopic pattern simulations have been performed by Bruker Daltonics program. Steady-state fluorescence spectra were recorded on a 10^{-6} M solution in acetonitrile with a Jobin Yvon Fluorolog3 spectrofluorometer, in the range 620–850 nm, using 5 nm grids for excitation and 5 nm for emission ($\lambda_{ex} = 600$ nm). The corresponding excitation spectrum has been collected in the range 350–700 nm, under an excitation wavelength of 750 nm, with 10 nm grids. No filters have been used. Time-resolved fluorescence measurements were carried out by a time-correlated single-photon counting (TCSPC) system (HORIBA Jobin Yvon), using a 405 nm pulsed laser diode and collecting the emission decay at the corresponding maximum emission wavelength (686 nm). The fluorescence decay profile was analyzed through decay analysis software (DAS6a HORIBA Scientific). The curve has been fitted with a monoexponential decay, with a final time decay of 2.4 ns. The quality of the fit was checked by examining the residual distribution having a χ^2 value of 1.4. Voltammograms were recorded at 25°C with a potentiostat-galvanostat Metrohm PGStat 204 in a conventional three-electrode cell; a platinum disk (~1 mm) was used as working electrode together with a platinum wire as auxiliary electrode. The reference electrode was Ag/AgNO$_3$ (0.01 M) in distilled acetonitrile (ACN) (Aldrich) (E_0 vs NHE = 0.548 V), and the Fc$^+$/Fc (ferrocenium/ferrocene) couple was used as external standard. The sample solutions were ~10^{-4} M in distilled anhydrous solvents, and dry tetra(n-butyl)ammonium tetrafluoroborate (TBATFB) (Aldrich) was used as the supporting electrolyte

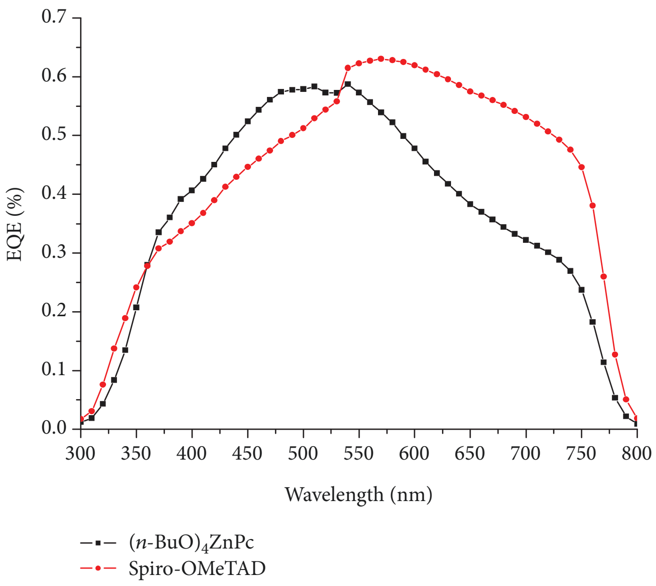

HTM	Integrated photocurrent (mA/cm^2)
(*n*-BuO)$_4$ZnPc	10.92
Spiro-OMeTAD	13.27

Figure 6: External quantum efficiency graphs of (*n*-BuO)$_4$ZnPc (black line) and Spiro-OMeTAD-based PSCs (red line).

Table 4: Calculated synthesis cost for 1 g of (*n*-BuO)$_4$ZnPc.

Synthetic steps	Reagents	Solvent	Purification	Total (wcs)	Total (bcs)
1	74.20	0.03	11.26	85.49	74.23

Table 5: Calculated synthesis cost for 1 g of (*n*-BuO)$_4$ZnPc with a bulk quotation of 1 kg of 4-n-butoxyphthalonitrile.

Synthetic steps	Reagents	Solvent	Purification	Total (wcs)	Total (bcs)
1	30.67	0.03	11.26	41.96	30.70

at 0.1 M. The solutions were previously purged for 10 minutes with nitrogen, and all measurements were performed under nitrogen. Cyclic voltammetry (CV) investigations were carried out at scan rates typically ranging from 0.05 to 2 Vs^{-1}. AFM images have been acquired in contact mode using a Keysight (formerly Agilent/MI) 5500 AFM with AppNano HYDRA6R-200N probes in air at room temperature and analyzed with the freely downloadable software WSxM 5.0 develop 8.4 December2016 [31].

Synthesis of (n-BuO)$_4$ZnPc (Mixture of Regioisomers). 200 mg of 4-*n*-butoxyphthalonitrile (1.0 mmol, 4 eq), 34 mg of zinc chloride (0.250 mmol, 1 eq), and a catalytic amount of 1,5-diazabiciclo[5.4.0]undec-5-ene (DBU) (1%mol, 1.7 μl) have been dissolved in 1 ml of N,N-dimethylethanolamine in a round bottom flask. The mixture has been refluxed for 15 hours and then cooled down, diluted with water, and filtered to obtain a solid which has been washed with water until the pH is neutral and the washings are colorless. The desired molecule has been purified by filtration on silica gel using dichloromethane and THF as eluents, affording 114 mg (yield 53%) of the target molecule as a shiny purple crystalline solid. ^{1}H NMR (THF-d8, ppm), δ: 1.21–1.25 (m, 12H; CH$_3$), 1.80–1.88 (m, 8H; CH$_2$), 2.08–2.16 (m, 8H; CH$_2$), 4.50 (m, 8H; OCH$_2$), 7.45–7.55 (m, 4H; macrocycle), 8.39–8.49 (m, 4H; macrocycle), 8.79–8.90 (m, 4H; macrocycle); IR (cm^{-1}): 2954–2870 (cluster), 1604, 1236, 1089, 1047, 742, UV-Vis (acetonitrile, nm,): 675, 354, MALDI-TOF (m/z) [M$^+$H$^+$] 866.3, elemental analysis: calcd = C (66.54%), N (12.93%), H (5.58%), found: C (66.07), N (13.05%), H (5.70%).

1.2. Device Fabrication. All the chemicals used for the device fabrication were purchased from Aldrich except methylamine (40% in methanol) which was purchased from Tokyo Chemical Industry Co. (TCI). TiO$_2$ paste was purchased from Dyesol. Methylammonium iodide (MAI) was synthesized by stirring 55.6 ml of methylamine (40% in methanol) with 60 ml of hydroiodic acid (57 wt% in water) in a 250 ml round bottom flask at 0°C for 2 h. The solvent was then evaporated at 50°C for 1 h using a rotary evaporator; the resulting solid was collected and stirred with ethanol for 30 minutes. It was then filtered and repeatedly washed with diethyl ether to obtain a white solid that has been dried at 60°C in a vacuum oven for 24 h.

The fluorine-doped tin oxide-coated SnO$_2$:F (FTO) conducting glass (15, Pilkington) substrates have been cut in 2.5×1.5 cm size. The substrates were then etched with Zn/HCl and cleaned properly. A hole-blocking layer was spin coated on FTO using a solution of titanium diisopropoxide bis(acetylacetonate) (TiDIP) (75% in 2-propanol) in ethanol and then annealed at 450°C for 30 minutes. A mesoporous titania layer was then deposited by spin coating using TiO$_2$ paste (DSL-90T TiO$_2$ NPs paste) diluted in ethanol (0.1 g of paste in 0.32 g of absolute ethanol) and calcinated at 500°C for 30 minutes. The TiO$_2$-deposited substrates were then treated with TiCl$_4$ for 30 minutes at 70°C, then rinsed, and annealed at 500°C for 30 minutes. The perovskite has been deposited using a two-step method. In the first step, 1 M solution of PbI$_2$ in a DMF : DMSO mixture (85 : 15 ratio) was spin coated on the substrates and annealed at 70°C for 45 min. The PbI$_2$-coated films were then immersed in a 10 mg/ml solution of MAI in 2-propanol for 30 seconds, resulting in the formation of dense black-brown MAPbI$_3$. The cells were further annealed at 90°C for 30 min. 40 μl of chlorobenzene solutions of (*n*-BuO)$_4$ZnPc (40 mg/ml) and Spiro-OMeTAD (72.3 mg/ml) was deposited by spin coating. 26.3 μl of Bis(trifluoromethane)sulfonimide lithium salt in acetonitrile (520 mg/ml), 29 μl of tris(2-(1H-pyrazol-1-yl)-4-tert-butylpyridine)-cobalt(III) tris(bis(trifluoromethylsulfonyl)imide)) in acetonitrile (300 mg/ml), and 19.2 μl of 4-tert-butilpyridine were added as dopants. Finally, 70 nm-thick gold-back contacts have been evaporated under pressure of 5×10^{-6} Torr. The active area was 0.09 cm^2, and a 0.04 cm^2 screen mask has been used during the measurements.

1.3. Photovoltaic Characterization. Photovoltaic measurements were made on a Newport system, composed of an Oriel I–V test station with an Oriel Sol3A simulator. The solar simulator is class AAA for spectral performance, uniformity of irradiance, and temporal stability. The solar simulator is equipped with a 450 W xenon lamp. The output power is adjusted to match AM1.5 global sunlight (100 mW·cm^2). The spectral match classifications are IEC60904-9 2007, JIC C 8912, and ASTM E927-05. I–V curves were obtained by applying an external bias to the cell and measuring the generated photocurrent with a Keithley model 2400 digital source meter. A 10 mV voltage step and a 40 ms photocurrent delay time were used. External quantum efficiency was calculated by measuring the I_{sc} of both the tested cell and a reference silicon cell at every wavelength, according to the following equation:

$$\text{EQE} = \left[\frac{I(\lambda)}{I_{\text{ref}}(\lambda)}\right]\text{EQE}_{\text{ref}}. \quad (1)$$

1.4. Computational Details. The structural, electronic, redox, and optical properties of (n-BuO)$_4$ZnPc, (t-Bu)$_4$ZnPc, and Spiro-OMeTAD have been investigated using ab initio simulations based on density functional theory (DFT). In detail, the calculations have been performed by using the ORCA suite of programs [20] in a localized-basis-set framework. Kohn-Sham orbitals have been expanded on a def2-TZVPP Gaussian-type basis set [32]. Fully decontracted def2-TZVPP/J has been also used as an auxiliary basis set for Coulomb fitting in a resolution-of-identity/chain-of-spheres (RIJCOSX) framework [33]. Molecular geometries have been fully optimized at the B3LYP level of theory [34, 35], including dispersion forces calculated by using the DFT-D3 approach [36]. Redox potentials of the molecules have been calculated by using the M06-2X functional [37], as discussed in detail elsewhere [21]. The molecules and their positive and negative ions have been embedded in an implicit CH_3CN solvent using the conductor-like polarizable continuum model (CPCM) [38] and fully optimized. The corresponding redox potentials have been calculated as ΔG values between neutral and charged species.

Data Availability

The phthalocyanine photoelectrochemical characterization data and the photovoltaic characteristics of the best-performing phthalocyanine-based and Spiro-based perovskite solar cells, used to support the findings of this study, are included within the article. The complete IV measurements can be furnished upon request. Furthermore, the experimental protocols to reproduce the synthesis and prepare the photovoltaic devices, the ^{1}H NMR chemical shifts, the IR main peaks, the UV-Vis absorption maxima, the MALDI-TOF molecular ion mass to charge ratio, the elemental analysis values of our molecule, and the computational details for the ab initio simulations are made available in the experimental section. The ^{1}H NMR full spectrum, MALDI spectrum, and anodic voltammogram of (n-BuO)$_4$ZnPc, used to confirm the molecular structure of our compound and support the findings of this study, are included in the supplementary materials.

Conflicts of Interest

The authors declare no competing financial interests.

Authors' Contributions

Gloria Zanotti and Giuseppe Mattioli contributed equally to the work.

Acknowledgments

G.Z. is thankful to the Ente Nazionale Energia e Ambiente (ENEA) and to the Italian Ministry of Foreign Affairs for a visitor post-doc fellowship to Ben Gurion University of the Negev. The authors are thankful to Sara Notarantonio for her precious assistance in the experimental work and in the electrochemical measurements. The research was funded in part by Israel's Ministry of National Infrastructures, Water and Energy Resources (grant no. 0399202/215-11-037) and by the Adelis Foundation.

Supplementary Materials

^{1}H NMR spectrum, MALDI spectrum, and anodic voltammogram of (n-BuO)$_4$ZnPc. Further details of the HTM cost analysis, consisting in two price tables and a synthesis flowchart. *(Supplementary Materials)*

References

[1] Z. Yu and L. Sun, "Recent progress on hole-transporting materials for emerging organometal halide perovskite solar cells," *Advanced Energy Materials*, vol. 5, no. 12, article 1500213, 2015.

[2] S. Ameen, M. A. Rub, S. A. Kosa et al., "Perovskite solar cells: influence of hole transporting materials on power conversion efficiency," *ChemSusChem*, vol. 9, no. 1, pp. 10–27, 2016.

[3] J. Yang, B. D. Siempelkamp, D. Liu, and T. L. Kelly, "Investigation of $CH_3NH_3PbI_3$ degradation rates and mechanisms in controlled humidity environments using in situ techniques," *ACS Nano*, vol. 9, no. 2, pp. 1955–1963, 2015.

[4] A. Kojima, K. Teshima, Y. Shirai, and T. Miyasaka, "Organometal halide perovskites as visible-light sensitizers for photovoltaic cells," *Journal of the American Chemical Society*, vol. 131, no. 17, pp. 6050-6051, 2009.

[5] W. S. Yang, B.-W. Park, E. H. Jung et al., "Iodide management in formamidinium-lead-halide–based perovskite layers for efficient solar cells," *Science*, vol. 356, no. 6345, pp. 1376–1379, 2017.

[6] L. Calió, S. Kazim, M. Grätzel, and S. Ahmad, "Hole-transport materials for perovskite solar cells," *Angewandte Chemie International Edition*, vol. 55, no. 47, pp. 14522–14545, 2016.

[7] M. Saliba, T. Matsui, J.-Y. Seo et al., "Cesium-containing triple cation perovskite solar cells: improved stability, reproducibility

and high efficiency," *Energy & Environmental Science*, vol. 9, no. 6, pp. 1989–1997, 2016.

[8] S. F. Völker, S. Collavini, and J. L. Delgado, "Organic charge carriers for perovskite solar cells," *ChemSusChem*, vol. 8, no. 18, pp. 3012–3028, 2015.

[9] P. Peumans, S. Uchida, and S. R. Forrest, "Efficient bulk heterojunction photovoltaic cells using small-molecular-weight organic thin films," *Nature*, vol. 425, no. 6954, pp. 158–162, 2003.

[10] K. Cnops, B. P. Rand, D. Cheyns, B. Verreet, M. A. Empl, and P. Heremans, "8.4% efficient fullerene-free organic solar cells exploiting long-range exciton energy transfer," *Nature Communications*, vol. 5, no. 1, p. 3406, 2014.

[11] O. A. Melville, B. H. Lessard, and T. P. Bender, "Phthalocyanine-based organic thin-film transistors: a review of recent advances," *ACS Applied Materials & Interfaces*, vol. 7, no. 24, pp. 13105–13118, 2015.

[12] G. Sfyri, C. V. Kumar, G. Sabapathi et al., "Subphthalocyanine as hole transporting material for perovskite solar cells," *RSC Advances*, vol. 5, no. 85, pp. 69813–69818, 2015.

[13] F. J. Ramos, M. Ince, M. Urbani et al., "Non-aggregated Zn(II)octa(2,6-diphenylphenoxy) phthalocyanine as a hole transporting material for efficient perovskite solar cells," *Dalton Transactions*, vol. 44, no. 23, pp. 10847–10851, 2015.

[14] J.-J. Guo, X.-F. Meng, J. Niu et al., "A novel asymmetric Phthalocyanine-based hole transporting material for perovskite solar cells with an open-circuit voltage above 1.0 V," *Synthetic Metals*, vol. 220, pp. 462–468, 2016.

[15] K. T. Cho, K. Rakstys, M. Cavazzini, S. Orlandi, G. Pozzi, and M. K. Nazeeruddin, "Perovskite solar cells employing molecularly engineered Zn(II) phthalocyanines as hole-transporting materials," *Nano Energy*, vol. 30, pp. 853–857, 2016.

[16] K. T. Cho, O. Trukhina, C. Roldán-Carmona et al., "Molecularly engineered phthalocyanines as hole-transporting materials in perovskite solar cells reaching power conversion efficiency of 17.5%," *Advanced Energy Materials*, vol. 7, no. 7, article 1601733, 2017.

[17] L. Edwards and M. Gouterman, "Porphyrins: XV. Vapor absorption spectra and stability: phthalocyanines," *Journal of Molecular Spectroscopy*, vol. 33, no. 2, pp. 292–310, 1970.

[18] F. Würthner, T. E. Kaiser, and C. R. Saha-Möller, "J-aggregates: from serendipitous discovery to supramolecular engineering of functional dye materials," *Angewandte Chemie International Edition*, vol. 50, no. 15, pp. 3376–3410, 2011.

[19] G. Mattioli, S. B. Dkhil, M. I. Saba et al., "Interfacial engineering of P3HT/ZnO hybrid solar cells using phthalocyanines: a joint theoretical and experimental investigation," *Advanced Energy Materials*, vol. 4, no. 12, article 1301694, 2014.

[20] F. Neese, "The ORCA program system," *Wiley Interdisciplinary Reviews: Computational Molecular Science*, vol. 2, no. 1, pp. 73–78, 2012.

[21] M.-H. Baik and R. A. Friesner, "Computing redox potentials in solution: density functional theory as a tool for rational design of redox agents," *The Journal of Physical Chemistry A*, vol. 106, no. 32, pp. 7407–7412, 2002.

[22] S. M. Ross, "Peirce's criterion for the elimination of suspect experimental data," *Journal of Engineering Technology*, vol. 20, pp. 38–41, 2003.

[23] J. Burschka, N. Pellet, S.-J. Moon et al., "Sequential deposition as a route to high-performance perovskite-sensitized solar cells," *Nature*, vol. 499, no. 7458, pp. 316–319, 2013.

[24] C. Roldán-Carmona, P. Gratia, I. Zimmermann et al., "High efficiency methylammonium lead triiodide perovskite solar cells: the relevance of non-stoichiometric precursors," *Energy & Environmental Science*, vol. 8, no. 12, pp. 3550–3556, 2015.

[25] H.-S. Kim and N.-G. Park, "Parameters affecting *I–V* hysteresis of $CH_3NH_3PbI_3$ perovskite solar cells: effects of perovskite crystal size and mesoporous TiO_2 layer," *Journal of Physical Chemistry Letters*, vol. 5, no. 17, pp. 2927–2934, 2014.

[26] H. J. Snaith, A. Abate, J. M. Ball et al., "Anomalous hysteresis in perovskite solar cells," *Journal of Physical Chemistry Letters*, vol. 5, no. 9, pp. 1511–1515, 2014.

[27] B. Chen, M. Yang, S. Priya, and K. Zhu, "Origin of *J–V* hysteresis in perovskite solar cells," *Journal of Physical Chemistry Letters*, vol. 7, no. 5, pp. 905–917, 2016.

[28] R. Scheer and H.-W. Schock, *Chalcogenide Photovoltaics: Physics, Technologies, and Thin Film Devices*, Wiley, 2011.

[29] E. A. Katz, A. Mescheloff, I. Visoly-Fisher, and Y. Galagan, "Light intensity dependence of external quantum efficiency of fresh and degraded organic photovoltaics," *Solar Energy Materials and Solar Cells*, vol. 144, pp. 273–280, 2016.

[30] T. P. Osedach, T. L. Andrew, and V. Bulović, "Effect of synthetic accessibility on the commercial viability of organic photovoltaics," *Energy & Environmental Science*, vol. 6, no. 3, pp. 711–718, 2013.

[31] I. Horcas, R. Fernández, J. M. Gómez-Rodríguez, J. Colchero, J. Gómez-Herrero, and A. M. Baro, "WSXM: a software for scanning probe microscopy and a tool for nanotechnology," *Review of Scientific Instruments*, vol. 78, no. 1, article 013705, 2007.

[32] F. Weigend and R. Ahlrichs, "Balanced basis sets of split valence, triple zeta valence and quadruple zeta valence quality for H to Rn: design and assessment of accuracy," *Physical Chemistry Chemical Physics*, vol. 7, no. 18, pp. 3297–3305, 2005.

[33] F. Weigend, "Accurate coulomb-fitting basis sets for H to Rn," *Physical Chemistry Chemical Physics*, vol. 8, no. 9, pp. 1057–1065, 2006.

[34] A. D. Becke, "Density-functional thermochemistry. III. The role of exact exchange," *The Journal of Chemical Physics*, vol. 98, no. 7, pp. 5648–5652, 1993.

[35] C. Lee, W. Yang, and R. G. Parr, "Development of the Colle-Salvetti correlation-energy formula into a functional of the electron density," *Physical Review B*, vol. 37, no. 2, pp. 785–789, 1988.

[36] S. Grimme, J. Antony, S. Ehrlich, and H. Krieg, "A consistent and accurate ab initio parametrization of density functional dispersion correction (DFT-D) for the 94 elements H-Pu," *The Journal of Chemical Physics*, vol. 132, no. 15, article 154104, 2010.

[37] M. Isegawa, F. Neese, and D. A. Pantazis, "Ionization energies and aqueous redox potentials of organic molecules: comparison of DFT, correlated ab initio theory and pair natural orbital approaches," *Journal of Chemical Theory and Computation*, vol. 12, no. 5, pp. 2272–2284, 2016.

[38] V. Barone and M. Cossi, "Quantum calculation of molecular energies and energy gradients in solution by a conductor solvent model," *The Journal of Physical Chemistry A*, vol. 102, no. 11, pp. 1995–2001, 1998.